

Fig. 1.40. A 4-element stacked-detector developed for high efficiency above 10 keV.

1.10 Polarization Studies

1.10.1 Introduction

The primary mission of the polarization studies program is to provide users with a high-brilliance, variably polarized x-ray beam. The polarized beams in sector 4 are produced by two separate undulators. To briefly review the main operational features, sector 4 has two branch lines, one for the “intermediate” (0.5 – 3 keV) and the other for the “hard” (> 3 keV) energy range. Variable polarization states are provided in the intermediate x-ray regime by a specialized circularly polarized undulator (CPU), while a planar undulator in combination with crystal optics has been used above 3 keV. A novel concept of spatially separating the beams from the insertion devices was successfully implemented for the first time at any synchrotron facility. The undulator axes are placed at a small angle ($270\ \mu\text{rad}$) with respect to each other. A dipole magnet between the devices introduces the angular deviation of the electron beam, so 30 m away, in the first optics enclosure (FOE), the two beams are separated by 8 mm. This is sufficient to use two horizontally deflecting mirrors in the

FOE to further separate the beams and deflect the intermediate energy x-ray beam down the beam pipe. This design enables simultaneous operation of both branch lines and thus more efficient utilization of the delivered beam. At the APS its success has been embraced in the design of several upcoming new beamlines (GM/CA-CAT, SER-CAT, SGX-CAT).

Since the last XFD Progress Report all the construction activities were completed. The beamlines were declared operational on July 15, 2001. Commissioning activities commenced with a vigorous schedule with the aim to achieve designed performance specifications by July 15, 2002. The bulk of the commissioning activities were directed towards the liquid-nitrogen-cooled double-crystal monochromator (DCM) and the torroidal mirror on the hard x-ray branch, and on the CPU and deflecting mirrors on the intermediate x-ray branch. By December 2001, the DCM operated according to theory, delivering 5×10^{13} photons/sec at 10 keV with Si (111) crystals. The torroidal mirror now focuses that flux to a spot size of $200\ \mu\text{m}$ by $120\ \mu\text{m}$ in the horizontal and vertical directions, respectively. The CPU is currently commissioned to operate in the circularly polarized mode with a switching

frequency of several minutes. The goal is to increase this frequency to 2 Hz. The degree of circular polarization was measured to be greater than 95% with a flux of 1×10^{13} photons/sec at 800 eV.

During the intense commissioning activities, whenever possible, cutting-edge experiments were simultaneously pursued. This approach resulted in publication of a *Physical Review Letter* article, “Enhanced interfacial magnetism in a Gd/Fe multilayer” in a record short time (Haskel et al., 2001). Concurrently, the emphasis on user support was given high priority as well, and, by July 15, 2002, already 28% of the beam time on the intermediate branch was awarded to independent investigators.

The development of state-of-the-art instrumentation and techniques using variable polarization resulted in several important contributions. They are described below and include probing magnetic interfaces in Fe/Gd with circularly polarized x-rays, measurement of magnetic ordering in SmNi_2Ge_2 , magnetic characteristics of transition-metal/semiconductor structures and, finally, study of the oxidation process in a class of magnetic tunnel junctions.

1.10.2 Probing Magnetic Interfaces with Circularly Polarized X-rays

Understanding chemical and magnetic properties of interfaces in layered systems is of great scientific and technological interest. For example, chemical interfacial roughness affects spin-polarized transport and related giant magneto-resistance effect in spin valves (Schad et al., 1998; Bae et al., 2000). The goal of this work is to quantify fundamental properties of buried magnetic interfaces, including the strength and extent of interlayer exchange coupling and magnetic roughness (Haskel et al., 2001). This quantitative information was obtained

by performing both x-ray resonance exchange scattering (XRES) (Hannon et al., 1988) and x-ray magnetic circular dichroism (XMCD) measurements on a Gd/Fe multilayer. The markedly different Curie temperatures of Gd (293K) and Fe (1024K) allow us to distinguish Gd “bulk” and interfacial regions by tuning the sample temperature. More generally it allows investigating proximity effects between low and high T_c ferromagnets at the atomic scale.

The origin of the magnetic sensitivity of the XRES and XMCD signals arises from the same fundamental process illustrated in Fig. 1.41. By tuning the x-ray energy to near a spin-orbit split absorption edge (resonance), angular momentum is transferred from the circularly polarized (CP) x-rays to the spin of the excited photoelectron with opposite x-ray helicities resulting in equal but opposite signs of spin polarization. The imbalance at the Fermi level in the density of unoccupied states between spin-up and -down states of a ferro (ferri)-magnetic material results in different absorption (scattering) cross sections for opposite helicities of incoming x-rays giving a measure of element-specific net magnetic moments.

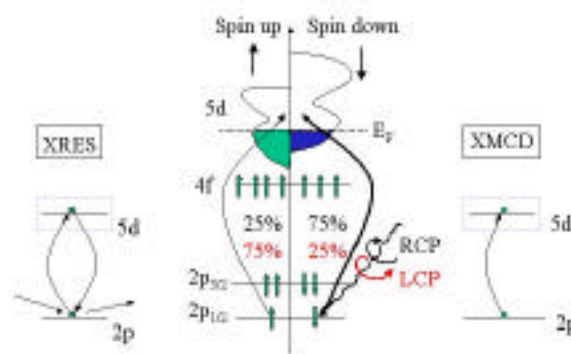


Fig. 1.41. Origin of magnetic sensitivity in the XRES (scattering) and XMCD (absorption) techniques.

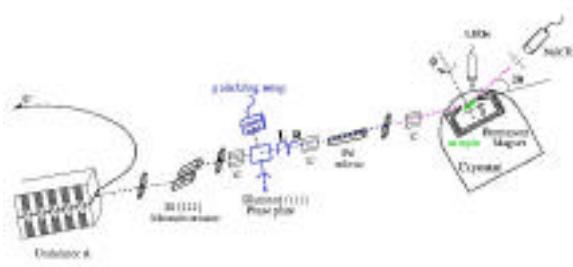


Fig. 1.42. Experimental setup.

The experiment, shown schematically in Fig. 1.42, was performed at the 4-ID-D insertion device beamline. A diamond quarter-wave plate is used to convert the x-rays' linear polarization into circular. The sample and a small permanent magnet ($B = 2.1$ kGauss) were placed inside a closed cycle He refrigerator mounted on the circle of a diffractometer. The applied field was oriented parallel to the sample's surface and in the scattering plane. X-ray resonance magnetic reflectivity (Sinha et al., 1988; Osgood III et al., 1999; Nelson, 1999), a special case of XRES, measures the difference cross section in the specular reflectivity of left- and right-CP x-rays. The difference in absorption coefficient between opposite helicities is measured by XMCD. The absorption was measured monitoring the Gd L fluorescence yield.

Figure 1.43 shows specular reflectivity curves as obtained by adding (top) and subtracting (bottom) scattered intensities for opposite helicities of the incoming CP radiation. The sum yields the "charge" reflectivity curve related to interference between waves scattered from charge density variations; the difference is due to interference between waves scattered from charge *and* magnetic density variations. Magnetization density profiles in the Gd layers were parameterized through variations in magnetic scattering factors and refined in a nonlinear least squares fitting of

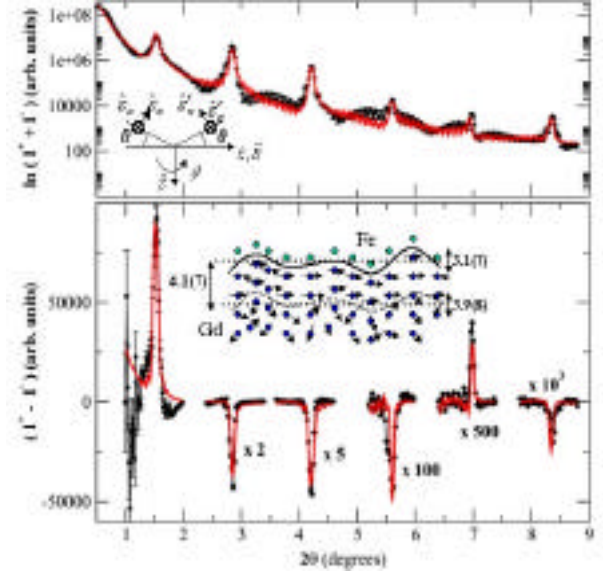


Fig. 1.43. Specular reflectivity curves across six multilayer Bragg peaks near the Gd L_2 edge ($E = 7929$ eV) at $T = 300$ K. Top inset shows scattering geometry and applied field direction. Bottom inset shows derived interfacial magnetic structure (all units Å) along with the fit to the data (red line).

the Born approximation cross section to the data. Best fits at 300 K (Fig. 1.43) show that Gd is paramagnetic except for a $4.1(7)$ Å region that remains magnetized near the Gd/Fe interface. This magnetization is induced by a strong antiferromagnetic (AF) interaction with the magnetically ordered Fe layer, in agreement with calculations by Camley (1989). The size of this region measures the spatial extent of the AF interaction at the interface and explains why Gd dominates the magnetization even above its bulk T_c .

The XMCD measurements are shown in Fig. 1.44. These data confirmed the size of the ordered Gd region obtained from the fit of the XRES spectra. At 300 K, the Gd layers retain 20% of their saturation magnetization, consistent with the magnetic

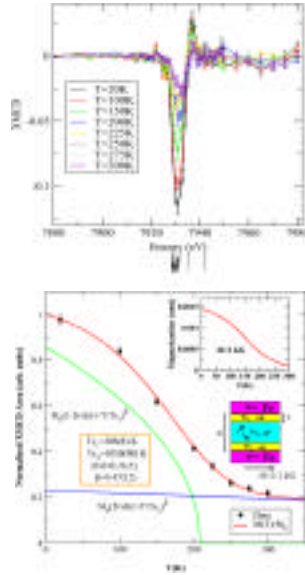


Fig. 1.44. XMCD data (top) and integrated area (points, bottom) at the Gd L₂ edge. Top inset in bottom figure shows SQUID magnetization data.

reflectivity result of 17% of the layer's volume remaining magnetized. The XMCD intensities are fitted as a superposition of interfacial and “bulk” regions with same saturation magnetization M_0 but variable T_c and volume fractions. The fit (red line) was convoluted with a Gaussian to account for disorder in the sputtered layers. Modeling gives 5.2 ± 1.2 Å for the magnetized region at 300K with an estimated $T_c = 1050(90)$ K. This T_c quantifies the strength of the AF interaction at the Gd/Fe interface; i.e., $J_{AF} J_{Fe} = 1000$ K. An enhanced T_c of 800 K was previously reported for one monolayer of Gd on a Fe(100) substrate (Taborelli et al., 1986).

In summary, we were able to quantify with high accuracy fundamental parameters characterizing a buried magnetic interface in a layered system. This includes the spatial extent and strength of interfacial exchange

coupling and interfacial magnetic roughness. Future work will be aimed at gaining a more complete understanding of the interfacial electronic and atomic structure. Spin-dependent x-ray absorption fine structure and XMCD combined with the x-ray standing wave technique should provide further insight into this question.

1.10.3 Fermi-Surface Nesting and Magnetic Ordering in SmNi_2Ge_2

It is not very common in solid-state physics to find an entire family of complex materials whose microscopic properties can be explained in terms of a few simple concepts. Rare-earth nickel germanides, however, do form such an isostructural group. Most of the moment-bearing members of this family undergo phase transitions at low temperatures below which the magnetic moments of the rare-earth ions spatially order in delicate arrangements. These intermetallics have a rather complicated tetragonal structure. As a result, the electronic structure of these compounds is quite intricate, and their magnetic ground state is determined by a subtle balance of various interactions, such as the long-range indirect exchange and single-ion crystal electric field effects. For almost all of the members of this group, the magnetic ordering wave vector has a fixed symmetry (along c^*) and is incommensurate to the lattice. Despite these complexities, calculations of electronic susceptibility can pinpoint the origin of this behavior. A pronounced topological nesting of the Fermi surface has been found to exist in these materials that fixes the magnetic wave vector to be of the form $q = (0, 0, q_z = 2k_F)$, where k_F is the Fermi wave vector. The wave vector typically ranges between 0.75–0.81 r.l.u. (Islam et al., 1999; Islam, 1999). The primary objective of this experiment is to study the magnetic structures of the Sm-

member (SmNi_2Ge_2), which have not been studied before, to see if they are consistent with the Fermi-surface nesting picture or not.

X-ray resonant exchange scattering (Hannon et al., 1988; Gibbs et al., 1988) provides a unique tool in determining the properties of such complex magnetic structures. In particular, its high reciprocal-space resolution, the ability to study very small-volume samples, and its element specificity provide information inaccessible via neutron measurements. Furthermore, XRES can be used to study neutron opaque compounds, such as the Sm compound studied in this experiment.

A rectangular crystal with dimensions $2.5 \times 0.9 \times 0.3 \text{ mm}^3$, cut with a face perpendicular to $[0,0,1]$ was used for this study. SmNi_2Ge_2 orders antiferromagnetically at $T_N = 17.9 \text{ K}$ and exhibits planar anisotropy above T_N . Another transition at $T_i = 11.8 \text{ K}$ is also clearly observed (Bud'ko et al., 1999). The XRES measurements were performed on the 1-BM-C bending-magnet beamline. The incident photon energy was tuned to the L_{II} edge (7.312 keV) of Sm in order to use the resonant enhancement. The $(0, 0, 6)$ reflection from a flat pyrolytic graphite crystal was used as the polarization analyzer. Integrated intensity were measured using a Ge solid-state detector, and the sample was cooled in a closed-cycle He refrigerator.

According to the nesting picture, the magnetic modulation vector is expected to lie along \mathbf{c}^* , with a \mathbf{q}_z value in the range mentioned above. A reciprocal lattice scan, at 8.0 K , revealed superlattice peaks with a wave vector at \mathbf{q}_z $(0, 0, 0.79)$. Figure 1.45 (left panel) shows an energy scan through the satellite peak at $(0, 0, 4.79)$.

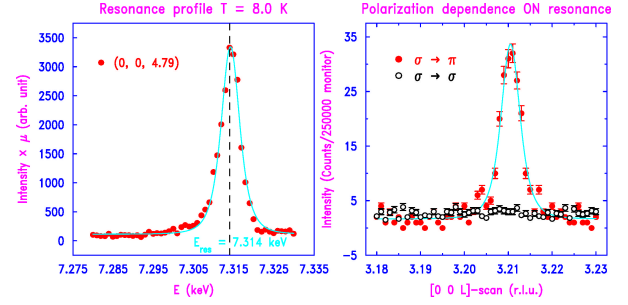


Fig. 1.45. Left: Energy scan through the Sm L_{II} -edge of superlattice peak. Right: Polarization analysis.

A strong resonant enhancement that occurs a few eV above the absorption edge, at 7.314 keV , with an enhancement factor of ~ 35 relative to the background $\sim 25 \text{ eV}$ below the edge. Polarization analysis (Fig. 1.45, right panel) revealed that the incident linear polarization perpendicular to the scattering plane (σ polarization) is completely rotated into the scattering plane (π polarization). The resonance and polarization properties indicate that the superlattice peak is magnetic in origin (Hannon et al., 1988; Gibbs et al., 1988; Hill & McMorrow, 1996).

Figure 1.46 summarizes the temperature dependence of the ordered phases. The integrated intensity of the magnetic peak (top panel) remains nearly temperature independent below T_i , suggesting saturation of the ordered Sm moments. Above T_i , the intensity decreases monotonically and disappears above T_N . The lower panel shows the variation of the magnetic wave vector with T . In the phase below T_N but above T_i , the modulation vector changes continuously with T approaching $\sim 0.775 \text{ r.l.u.}$ near T_N , indicating the *incommensurate* nature of the ordering, consistent with the Fermi-surface nesting picture. Below T_i , however, the structure is characterized by a temperature-

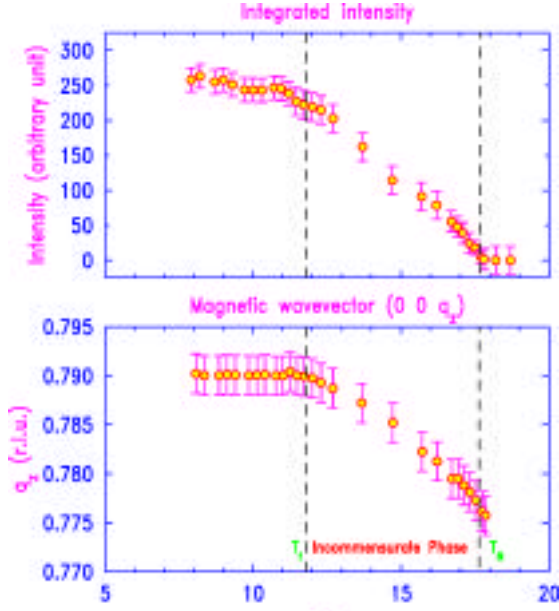


Fig. 1.46. Temperature dependence of the integrated intensity (upper) and position (lower) of the magnetic peak.

independent $\mathbf{q} = (0, 0, 0.79 \pm 0.002)$, suggesting a long-period ordered phase. The temperature at which q_z reaches this value is identified as T_i with a concomitant near saturation of the intensity, which is 11.8 ± 0.2 K.

The anisotropy of moment directions was also studied by measuring the intensity of a number of magnetic peaks. The intensity variation as a function of \mathbf{q} suggested that the ordered Sm moments are essentially confined to the tetragonal basal plane. Although near T_N , the moments are free to rotate in the basal plane forming a helix (Fig. 1.47, left side) since the in-plane anisotropy is negligible, below T_i the moments may lock in along some crystallographic direction within the plane (Fig. 1.47, right side).

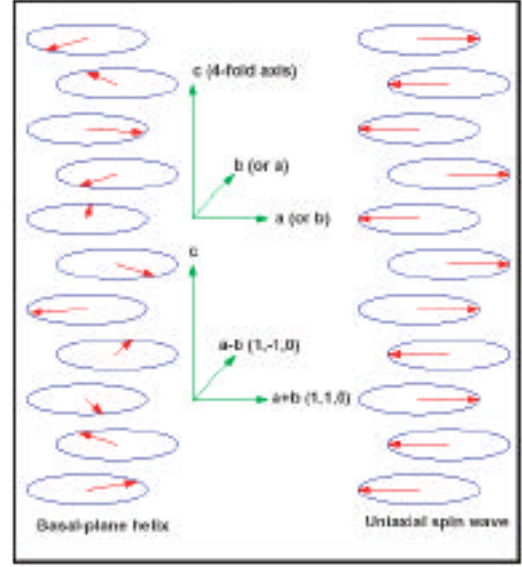


Fig. 1.47. Possible spin wave structures.

In summary, the primary result of this work is that the magnetic structures of the Sm-member of the $R\text{Ni}_2\text{Ge}_2$ series conform to the topological nesting of the Fermi surface. SmNi_2Ge_2 orders in an *incommensurate* antiferromagnetic structure characterized by $\mathbf{q} = (0, 0, q_z)$. The value of q_z is T -dependent and approaches ~ 0.775 r.l.u. near $T_N = 17.8 \pm 0.2$ K. The ordered moments are confined to the basal plane, as is in the case of a basal-plane helix or a plane wave.

1.10.4 Magnetic Characteristics of Transition-Metal/Semiconductor Structures

With the advent of spin-based electronics ("spintronics") the integration of thin magnetic layers with semiconductors is a priority (Prinz, 1995). The physics behind spintronics relies on the ability to inject spin-polarized currents into magnetic heterostructures. One such system that has shown very promising results is based on III-V materials (Kikkawa & Awschalom,

1999). It has been observed that spin injection into semiconductor quantum wells can retain spin coherence over length scales of 100 μm . This is several orders of magnitude more than is capable for transition-metal-based devices. The current magnetic semiconductors however suffer from low spin polarization and ordering temperatures. Transition metals are more favorable but are potentially incompatible with semiconductors (Xu et al., 1999) since alloying at the semiconductor/transition metal interface results in the formation of a magnetically dead layer and strongly modified magnetic anisotropy (see Fig. 1.48).

To date the detailed nature of the dead layer and anisotropy are not well understood. Using a combination of polarized soft x-ray techniques (XMCD and XRMS), a study has been initiated to understand the fundamental contributions to the magnetic characteristics of growing transition metals Fe, Co and Ni on Ge and GaAs. The samples were grown by molecular beam epitaxy at the University of Arizona. The high quality of the sample growth was monitored during growth with RHEED. The transition metals have been grown in a wedge format ranging in thickness from 0 \AA to 50 \AA and capped with a 35 \AA Au protective layer. This sample provides continuous access to the whole thickness range which is necessary for a precise mapping of the onset of magnetic order.

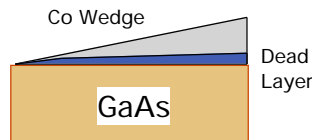


Fig. 1.48. An illustration of the magnetic dead layer that forms at the interface inhibiting such spin-injecting devices.

The XMCD technique is specifically powerful within this arena because of the accessibility to the 3d states of the transition metals (Thole et al., 1992). Figure 1.49 indicates the separate absorption spectra taken with opposite magnetic field directions. The resultant difference is the XMCD signal. XMCD is both element and site specific and has the ability to separate the constituent parts of the total magnetic moments into the spin and orbital contributions (Thole et al., 1992). This offers the possibility to assess the theoretical efforts of developing magnetic anisotropic energy models currently describing ultrathin transition magnetic materials on semiconductor substrates (Cabria et al., 2000).

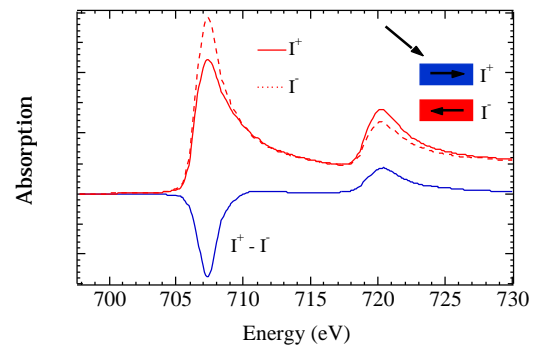


Fig. 1.49. Polarization dependent absorption spectrum measured at the Fe L edge. This contrast is a powerful tool for element by element magnetic analysis. The inset shows the orientation of photon helicity and magnetization for each measurement.

Results for the Co wedge on GaAs at both 300K and 90K are shown in Fig. 1.50 as a function of Co thickness. The onset of order is seen by a nonzero XMCD signal at 8 \AA Co (4 monolayers). The intensity grows with increasing Co material but is not linear. Figure 1.51 indicates the rate of signal change with respect to Co thickness at both 300K and 90K. There is a significantly different rate of dichroism change at lower

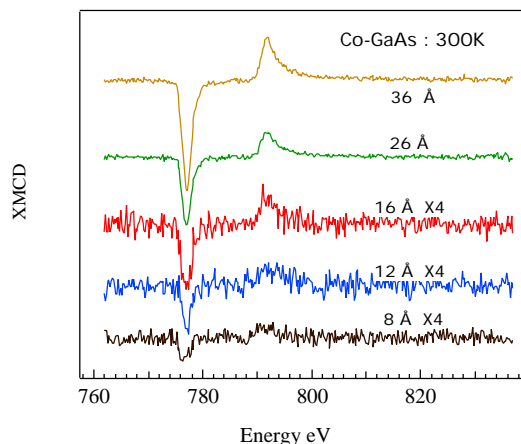


Fig. 1.50. Series of XMCD with total electron yield at 300K with different Co coverages. The XMCD signal shows the onset of magnetic order at 4 monolayer (ML) coverage.

Co coverage. This indicates an interface environment with a lower T_C . Primarily, dichroism at such low coverages has not been seen or the magnetic character been investigated to such degree. Here we see effects of the dead layer at very low coverages. Interestingly, the onset of dichroism shifts to lower Co coverage at lower temperatures, from ~ 4 monolayers (ML) at room temperature to ~ 2.6 ML at 90K.

Figure 1.52 shows a typical rocking curve spectra taken with 20 Å of Co. The spectrum is composed of two primary parts, the specular and diffuse signals. The ratio of which give an understanding of the physical and related magnetic roughness at the interface. Analysis of the sum and XMCD signals provides a measure of the chemical and magnetic perpendicular roughness (σ) near 2 Å. The narrow width indicates a long-range order in the plane of the film.

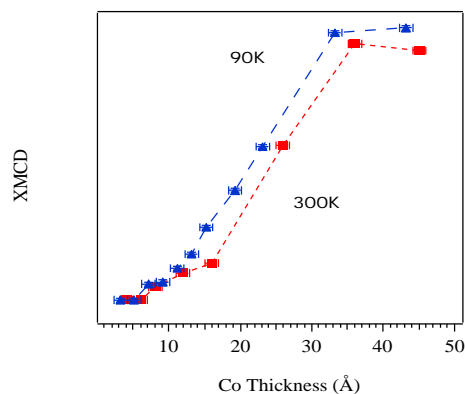


Fig. 1.51. Thickness dependence of Co grown on GaAs. Note how the onset drops to 2.4 ML at 90K. More detailed analysis of the spin and orbital moments will provide insight into the thickness dependence.

Application of the aforementioned techniques on such high-precision samples offers unprecedented information about the intrinsic characteristics of transition metals on semiconductors. Understanding the fundamental issues pertaining to such interfaces may refuel interest in such spin-injection devices.

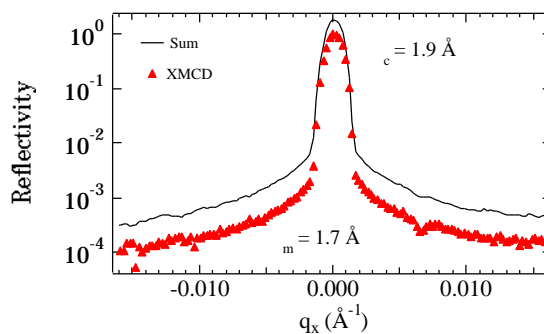


Fig. 1.52. X-ray resonant magnetic diffuse scattering at the Co L_3 edge. Analysis of the sum and XMCD signals provides a measure of the chemical and magnetic perpendicular roughness (σ). The narrow width indicates a long-range order in the plane of the film.

1.10.5 Linking the Oxidation Process with Magnetic Properties of Magnetic Tunnel Junctions

With the discovery of large spin-dependent tunneling in structures consisting of two ferromagnetic layers separated by a thin (~ 10 Å) insulating spacer (Moodera et al., 1995), new possibilities are evident for a variety of spin-based electronic devices. This system has potential applications from sensors to nonvolatile magnetic random access memory (MRAM), but many facets of the underlying structure and its impact on device physics are not well understood. Aluminum oxide (Al_2O_3) is the most widely used insulating spacer and is formed by the thermal or plasma oxidation of Al metal after deposition. Oxidation of thin layers in proximity to transition-metal-based ferromagnets always leads to the potential for oxide formation in neighboring layers (Keavney et al., 2001; Seve et al., 2001). The goal of this study is to use the element- and interface-specific capabilities to track the oxidation process and changes due to thermal annealing.

A series of wedge-shaped structures were prepared by the Physical Sciences Research Laboratories at Motorola. Samples are grown using ion beam deposition, and the structure is shown in Fig. 1.53. The Al layer is deposited as a wedge from 5 - 9 Å and is plasma oxidized before deposition of the top NiFeCo layer. It is expected that in the region < 9 Å the bottom layer will show a linear progression of the oxide into the CoFe layer, but, as described in the text below, the real structure is quite different.

As the plasma oxidation is initiated, it proceeds along the following course. For the 9 Å end of the wedge, a stable film of Al_2O_3

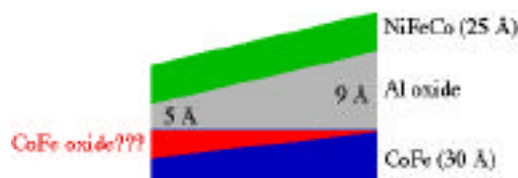


Fig. 1.53. Diagram of magnetic tunnel junction trilayer sample, which has been oxidized for an optimal Al oxide thickness of 9 Å.

is formed (see Fig. 1.54). The Al K-edge absorption is consistent with formation of a polycrystalline oxide layer. In the range of 9-7 Å, the Al K-edge spectra evolves to a metastable state consistent with the presence of excess oxygen in the layer and remains unchanged for all thickness < 7 Å. While the Al is still in a 3^+ oxidation state, the interstitial oxygen modifies the 3p density of unoccupied states (see Fig. 1.54). The trapping of excess oxygen in the Al layer reduces the oxide in the CoFe layer and only for an Al thickness < 7 Å does a large oxide component appear in the bottom layer (see Fig. 1.55).

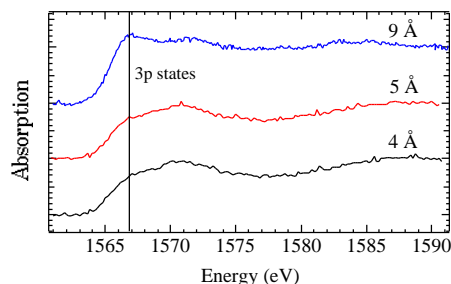


Fig. 1.54. Al K edge x-ray absorption spectra as a function of oxide thickness. The main feature denoted by the line is related to the 3p density of unoccupied states. In the region of 9-7 Å this feature decreases in intensity as interstitial oxygen modifies the band structure.

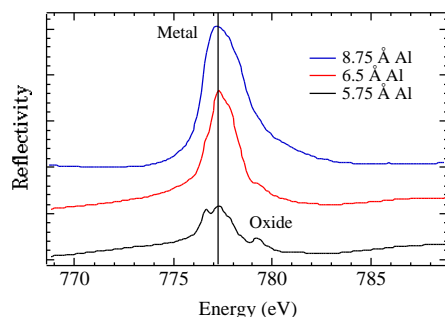


Fig. 1.55. X-ray resonant reflectivity at the Co L_3 edge. The features clearly indicate the oxidation of the CoFe underlayer at the thin end of the Al oxide wedge.

Determination of element-specific magnetic properties is accomplished using XMCD (Chen et al., 1995). The absorption and reflectivity from the sample is directly dependent on the orientation of the elements magnetic moment with respect to the helicity of the incident photon beam. This technique can be used to either monitor magnetic response to an applied magnetic field or more detailed analysis of the energy-dependent XMCD to determine spin and orbital magnetic moments. For this system, the most interesting aspect is the magnetic hysteresis of the two layers. The bottom layer is exchanged biased by an underlying IrMn antiferromagnet. Before the annealing to 200°C in a 100 Oe applied field, the hysteresis consists of a large saturation field (1 kOe) and small remanent moment (10% of saturation). After annealing, the CoFe layer has 100% saturation at zero field and large exchange bias. The hysteresis of the top NiFeCo layer is shown in Fig. 1.56. Annealing the sample results in a dramatic decrease of the coercivity from 65 G to 19 G and slight shift of the loop to negative field direction. The coercive field is constant across the entire edge, but the coupling field varies due the changing dipolar coupling to the CoFe underlayer.

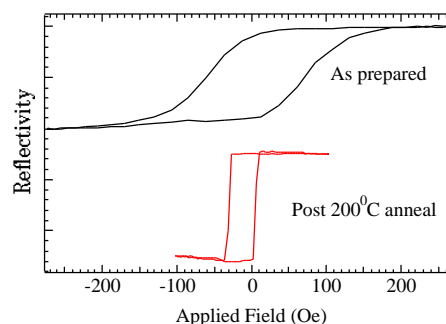


Fig. 1.56. Element-specific hysteresis measured at the Ni L_3 edge. This determines directly the field response of the top NiFeCo magnetic layer. Clearly the annealing process has a dramatic effect on the magnetic switching.

One of the major questions is the change in the structure after the field anneal. Are changes in the magnetic response due to structural or magnetic changes? Measurements of the x-ray magnetic resonant diffuse scattering (Freeland et al., 1999; Haskel et al., 2001) allow the determination of chemical and magnetic interface structure in a layer-by-layer fashion. Scattering at the Mn, Co, and Ni L_3 edges, provide element (and therefore layer) specific information. A Ni rocking curve measured at a $q_z = 0.3 \text{ \AA}^{-1}$ is shown in Fig. 1.57. Analysis of the rocking curves show that the preanneal structure is characterized by a conformal roughness ($\sigma = 3 \text{ \AA}$ and $\lambda = 300 \text{ \AA}$) propagating through the whole structure. After the anneal, there is no change, indicating that the structure is stable under these conditions and all magnetic changes are due solely to dipolar fields from the alignment of the random domains on the IrMn exchange bias layer.

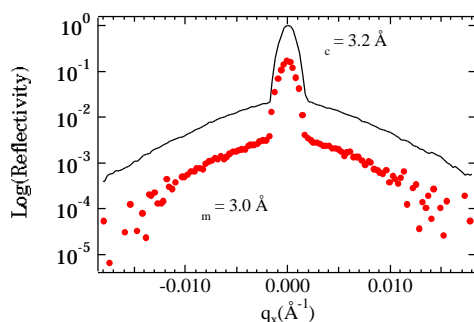


Fig. 1.57. X-ray resonant magnetic diffuse scattering at the Ni L_3 edge (852 eV). The chemical scattering (solid line) is connected to the structure of the chemical interface while the magnetic diffuse (red dots) is related to chemical and magnetic disorder.

1.11 References

- A. Allen, J. Ilavsky, G. G. Long, J. S. Wallace, C. C. Berndt, and H. Herman, *Acta Mater.* **49**, 1661-1675 (2001).
- S. Bae, J.H. Judy, W.F. Egelhoff Jr., and P.J. Chen, *J. Appl. Phys.* **87**, 6980 (2000).
- M.J. Bedzyk, G.M. Bommarito, and J.S. Schildkraust, *Phys. Rev. Lett.* **62** (1989).
- P. Bosecke and O. Diat, *J. Appl. Crystallogr.* **30**, 867-871 (1997).
- W. Bras and A. J. Ryan, *J. Appl. Crystallogr.* **30**, 816-821 (1997).
- S.L. Bud'ko, Z. Islam, T.A. Wiener, I.R. Fisher, A.H. Lacerda, and P.C. Canfield, *J. Magn. Magn. Mat.* **205**, 53 (1999).
- I. Cabria, H. Ebert and A. Ya. Perlov, *Europhys. Lett.* **51**, 209 (2000).
- R.E. Camley, *Phys. Rev. B* **39**, 12316 (1989).
- C.T. Chen, Y.U. Idzerda, H-J. Lin, N.V. Smith, G. Meigs, E. Chaban, G.H. Ho, E. Pellegrin and F. Sette, *Phys. Rev. Lett.* **75**, 152 (1995).
- Y.S. Chu, C. Liu, D.C. Mancini, F. De Carlo, A.T. Macrander, B. Lai, and D. Shu, *Rev. Sci. Instrum.* **73**, 1485 (2002).
- D.H. Cole, K.R. Shull, L. Rehn, and P. Baldo, *Macromolecules* **32**, 771 (1999).
- C.B. Collins, F. Davanloo, M.C. Iosif, R. Dussart, J.M. Hicks, S.A. Karamian, C.A. Ur, I.I. Popescu, V.I. Kirischuk, J.J. Carroll, H.E. Roberts, P. McDaniel, and C.E. Crist, *Phys. Rev. Lett.* **82**, 695 (1999).
- F. DeCarlo, P. Albee, Y.S. Chu, D.C. Mancini, B. Tieman, and S.Y. Wang, *SPIE Proc. Vol.* **4503** (2002) p. 1.
- D.E. Eastman, C.B. Stagaescu, G. Xu, P.M. Mooney, J.L. Jordan-Sweet, B. Lai, and Z. Cai, *Phys. Rev. Lett.* **88**, 156101 (2002).
- P.G. Evans, E.D. Isaacs, G. Aeppli, Z. Cai, B. Lai, *Science* **295**, 1042 (2002).
- J.W. Freeland, K. Bussmann, Y.U. Idzerda, and C.-C. Kao, *Phys. Rev. B* **60**, R9923 (1999).
- D. Gibbs, D.R. Harshman, E.D. Isaacs, D.B. McWhan, D. Mills, and C. Vettier, *Phys. Rev. Lett.* **61**, 1241 (1988).
- J.P. Hannon, G.T. Trammell, M. Blume, and D. Gibbs, *Phys. Rev. Lett.* **61**, 1245 (1988).
- D. Haskel, G. Srajer, J.C. Lang, J. Pollmann, C.S. Nelson, J.S. Jiang, S.D. Bader, *Phys. Rev. Lett.* **87**, 207201 (2001).
- J.P. Hill and D.F. McMorrow, *Acta Crystallogr. A* **5**, 236 (1996).
- S. Hosokawa, H. Sinn, F. Hensel, A. Alatas, E. E. Alp, and W.C. Pilgrim, *J. Non-Cryst. Solids*, in press.
- Z.W. Hu, B. Lai, Y.S. Chu, Z. Cai, D.C. Mancini, B.R. Thomas, and A.A. Chernov, *Phys. Rev. Lett.* **87**, 148101 (2001).